On-chip readout plasmonic mid-IR gas sensor

Qin Chen[1]*, Li Liang[1], Qilin Zheng[1], Yaxin Zhang[2] and Long Wen[1]*

Gas identification and concentration measurements are important for both understanding and monitoring a variety of phenomena from industrial processes to environmental change. Here a novel mid-IR plasmonic gas sensor with on-chip direct readout is proposed based on unity integration of narrowband spectral response, localized field enhancement and thermal detection. A systematic investigation consisting of both optical and thermal simulations for gas sensing is presented for the first time in three sensing modes including refractive index sensing, absorption sensing and spectroscopy, respectively. It is found that a detection limit less than 100 ppm for CO_2 could be realized by a combination of surface plasmon resonance enhancement and metal-organic framework gas enrichment with an enhancement factor over 8000 in an ultracompact optical interaction length of only several microns. Moreover, on-chip spectroscopy is demonstrated with the compressive sensing algorithm via a narrowband plasmonic sensor array. An array of 80 such sensors with an average resonance linewidth of 10 nm reconstructs the CO_2 molecular absorption spectrum with the estimated resolution of approximately 0.01 nm far beyond the state-of-the-art spectrometer. The novel device design and analytical method are expected to provide a promising technique for extensive applications of distributed or portable mid-IR gas sensor.

Keywords: gas sensor; mid-IR; on-chip; surface plasmon resonance; spectroscopy

Introduction

There are growing interests for gas sensing such as greenhouse gas monitoring[1], indoor air quality supervision[2], automobile tail gas discharge detection[3], toxic or flammable gases detection[4], breath diagnostics[5], industrial production[6], etc. So far, several major approaches have been developed[7], including electrochemical sensors[8], calorimetric sensors[9], acoustic sensors[10] and optical sensors[11]. Optical methods[12], in particular in the mid-IR range, are usually straightforward and have short response time, long lifetime, high sensitivity and selectivity. Generally, there are three mechanisms for optical gas sensing, including (i) refractive index (RI) sensing based on the real part of gas RI[13], (ii) non-dispersive infrared (NDIR) absorption sensing based on the imaginary part of gas RI[14], and (iii) spectroscopy based on the gas molecular spectral fingerprint[15]. The RI sensing method allows for characterization of nonreactive gases and very compact sensor

design. However, this technique such as surface plasmon resonance (SPR)[16] sensors that are widely used in liquid and solid detection suffers sensitivity issues for gas sensing due to the low RI difference (~10^{-4} RIU) between various gases. For example, a localized SPR spectroscopy was developed with a detection limit level about 3×10^{-4} RIU that only showed measurable signal between pure Ar and He[17]. An air-slot photonic crystal nanocavities was used to enhance the light-gas interaction, but a similar RI detection limit of 10^{-5} RIU was estimated considering a 3 pm spectral measuring resolution[18]. As a result, some signal amplification techniques were developed. For example, silicon glycol copolymer was used in a standard SPR setup to enrich halothane and reduce the detection limit down to 80 ppm, where both thickness and RI of the copolymer are affected by the gas absorption[19]. Similarly, Pd[20], carbon nanotube[21], and SnO_2 microspheres[22] are also widely used to increase the RI variations by chemical reactions. In contrast, NDIR absorption sensing method is

more popular[23]. This technique is based on the Beer–Lambert Law, and thus the sensitivity can be increased by simply lengthening the optical path for light-gas interaction. For example, a detection limit for formaldehyde of 120 pptv was demonstrated by using an antimonide laser and a 1 m base-length cell with a multipass path lengths of 100 m by mirrors[24]. Ethyl chloride gas at a 5 ppm concentration level was detected by using a distributed-feedback quantum cascade laser (QCL) coupled with a silica capillary with a length of 4 m[25]. Instead of laser sources, the NDIR sensing system can also be built with a broadband source, narrowband filter and detector. For example, a detection limit of 50 ppm was predicted in an ellipsoid gas cell system with a LED source and PbSe detector[26]. No matter which configuration, due to the low molecular absorption cross-sections of mid-IR vibrations (10^{-20} cm^2), the whole system is bulky to ensure a high sensitivity and therefore limited for integrated applications.

Recently, nanophotonic structures have attracted extensive interests in optical sensing fields[27,28]. Novel designs and excellent sensing performances have been demonstrated due to their remarkable electromagnetic field enhancement[29], spectral manipulating[30], chirality[31] and phase[32] engineering, etc. Some pioneered works have also explored mid-IR gas sensing. By manipulating the spatial electromagnetic field distribution, a detection limit of 60000 ppm for CO_2 was demonstrated in a 4 mm long gas cell device containing a metal microstructure array, which provides a 1100 times absorption enhancement in the optical path together with a porous metal-organic framework (MOF)[33]. By engineering the emission spectrum, an NDIR sensor with a narrowband thermal emitter based on plasmonic crystal was demonstrated with a detection limit of 10000 ppm for CO_2 in a 7.5 mm gas cell[34]. Similarly, the detection wavelength can also be engineered by integrating microstructure filters with the detector[23,25], in which case it can form a sensing system with a low-cost broadband source. Although all these works demonstrated promising developments, the nanophotonic mid-IR gas sensors still suffer some major issues, 1) the detection limit is too high for low concentration gas detection, 2) the linewidth of either emitter or detector is too large with a quality (Q) factor <10 and limits the device figure of merit, 3) a lack of spectroscopic analysis, and 4) the gas cell is still not compact.

In this article, a novel mid-IR gas sensor consisting of a narrowband plasmonic absorber integrated with a thermal detector is proposed to address these issues. The shallow metal grating structure is adopted and found to provide a high Q factor resonance and strongly localized resonant field, which ensures a high sensitivity even at a limited light-gas interaction length. The combination of the optical resonator and thermal detector offers on-chip direct readout for portable gas sensors. Thoughtful investigation based on both optical and thermal simulation reveals the significant enhancement on the sensitivity via both SPR and MOF. The on-chip spectroscopy with an ultrahigh spectral resolution is also demonstrated by using a narrowband sensor array with the help of compressive sensing algorithm. In addition, the size effect existing in most periodic plasmonic structure is investigated considering the practical applications and a potential solution is discussed.

Mechanism and design

Mechanism

Conventionally, the gas sensing system needs a bulky gas chamber to ensure a strong light-gas interaction for low detection limit[36-38]. As is well known, micro-resonators are usually used to enhance the light-matter interaction[30], which is able to reduce the sensor dimensions for distributed or low-load platform while keeping a high performance. To construct a high sensitivity, compact gas sensor for on-site application, it is important to integrate separated elements into a single multi-functional component. Moreover, the performance is maintained or even improved by an optimal combination of different functions. Inspired by the previous work on microfluidic integrated metamaterial 'flowing through' sensor[29] and color routing metal scatters integrated silicon optoelectronic device[39], a novel mid-IR gas sensor is proposed as shown in Fig. 1(a), where an optical resonator such as metal covered subwavelength periodic gratings integrates with thermal resistance material. It can be seen as a monolithic combination of a resonant sensor and a thermal detector. The incident light is coupled to the surface resonant mode by the gratings and the on-resonance absorption generates heat mainly in metal, which is transmitted to the adjacent thermal resistive materials. The operating mechanism as shown in Fig. 1(b) is that the environment gas variation modifies the light absorption of the resonator and thus changes the temperature of the sensing element with a result of an electric signal by the thermal resistance of VO_2. As a result, it is possible to achieve chip

scale gas sensing system, possessing a compact device dimension due to the enhanced light-matter interaction and the novel combination of sensing and transducing elements.

For a high sensing performance, it needs to optimize both optical and electrical design to integrate efficiently. From the optical sensing perspective, the larger change of the light absorption at the same gas concentration variation, the stronger the detection signal. To achieve this, a resonator with a narrowband and efficient absorption is required in a broadband wavelength range. The wavelength selective detection also increases the gas selectivity. From the electrical transducing perspective, although the photodetectors based on compound semiconductors usually have high detectivity in the mid-IR range[40], it is too expensive and not compatible to the CMOS process. Thermal detectors with a reasonably good sensitivity attract lots of attention due to the simplicity and low cost[41]. Obviously, the more efficient of the heat induced resistance variation, the stronger electric current signal, i.e. the device is more sensitive. To achieve this, a thermal resistance material with a large temperature coefficient of resistance and low 1/f noise such as VO_2 is chosen and fabricated adjacent to a thermal source. To connect optical and electrical perspectives, the on-resonance light absorption is converted to photocurrent in such a $Au/Si_3N_4/VO_2/Si_3N_4$ multilayer thermal resistor.

However, it is not straightforward to achieve a narrowband resonant absorption with a large Q factor. In fact, the Q factors are very low for most plasmonic and metamaterial absorbers based on periodic metal structures although they usually have strong light-matter interaction[29,42]. For example, the microfluidic metamaterial sensor has a resonant absorption with a Q factor less than 10[29] and a SPR photodetector has a resonant absorption with a Q factor about 15[43]. Fano resonance[44], asymmetrical unit cell[45] and even gain material[46] were used to increase the Q factor. Generally, the Q factor associates with radiation loss and absorption loss in a resonant system[16,47]. It is important to reduce both losses to realize a high Q factor. The absorption is associated with the ohmic loss. Although TiN, AZO and graphene have been investigated as alternative plasmonic materials, noble metals are still the main materials to construct plasmonic or metamaterial absorbers, where Au and Ag have relatively low absorption loss. On the other hand, the radiation loss can be reduced to zero in a flat layered structure. Therefore, the radiation loss in a resonator configuration as

shown in Fig. 1(a) can be suppressed by decreasing the grating depth. However, the grating depth cannot be too small because the light absorption of such a resonator depends on the optical coupling. Based on the coupled mode theory, the maximum absorption occurs at the critical coupling condition when the radiation loss equals the absorption loss[26]. Therefore, a systematic investigation is required to optimize the optical design of gas sensor.

VO_2 is a typical thermal resistance material, which has attracted great interest for several decades due to its metal-semiconductor transition around 60°C (Supporting Information Fig. S1). It has been widely used in infrared detectors[48,49]. For example, the commercial VO_2 infrared detector can detect a temperature variation as low as 30 mK[50]. To enable the on-chip direct readout of the mid-IR gas sensing signal, VO_2 is deposited close to the metal layer and is separated by a Si_3N_4 layer to avoid shortcut as shown in Fig. 1(a). Apart from the electric insulation, it is also important to reduce the thermal conductance of the transducer. It can be realized by fabricating the $Au/Si_3N_4/VO_2/Si_3N_4$ multilayer stack on a silicon membrane by removing the silicon handle layer at the back of a silicon-on-insulator (SOI) wafer. It is important to optimize the device structure by the thermal modeling to reduce heat dissipation and ensure a large variation of electric resistance.
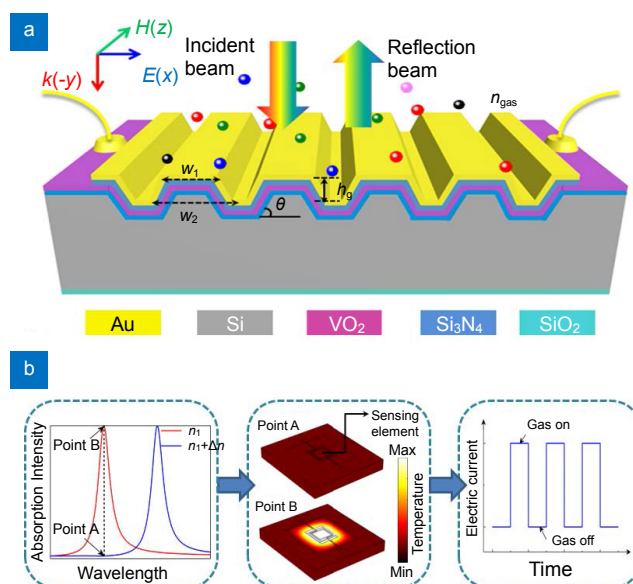

Fig. 1 | (a) Schematic of a multilayer stack ($Au/Si_3N_4/VO_2/Si_3N_4$) coated silicon gratings for on-chip gas sensing. (**b**) Sensing mechanism. The variation of gas concentration induces an increase/decrease of light absorbance of the microstructures and then causes a temperature increase/decrease, which generates an electrical signal via VO_2.

Optical design

The optical model of the gas sensor is shown in Fig. 1(a), where the silicon gratings with slope sidewalls ($\theta = 54.7°$) were used to consider the practical fabrication process by wet etching. The numerical simulation is based on the finite-difference time-domain algorithm and the material parameters are from literatures[51]. First, the periodic boundary condition with a plane wave source is used to model the optical properties of infinite periodic structure. The structure dimensions are optimized to achieve a single resonant peak in the mid-IR absorption spectra with low background absorption. As shown in Fig. 2(a), the resonant wavelength λ_r increases with the environmental RI n_{gas}, where $\lambda_r = 3300$ nm at $n_{gas} = 1$ and $\lambda_r = 3333$ nm at $n_{gas} = 1.01$. Therefore, the high sensitivity $S = 3300$ nm/RIU is achieved. The large sensitivity is associated with the strong confinement of the resonant mode on the surface of the sensor as shown in Fig. 2(c), which provides a strong near-field light-gas interaction. Moreover, the absorption peaks are narrow with an average FWHM of approximately 13 nm and consequently the Q factors are around 250 as shown in Fig. 2(b), which is one order
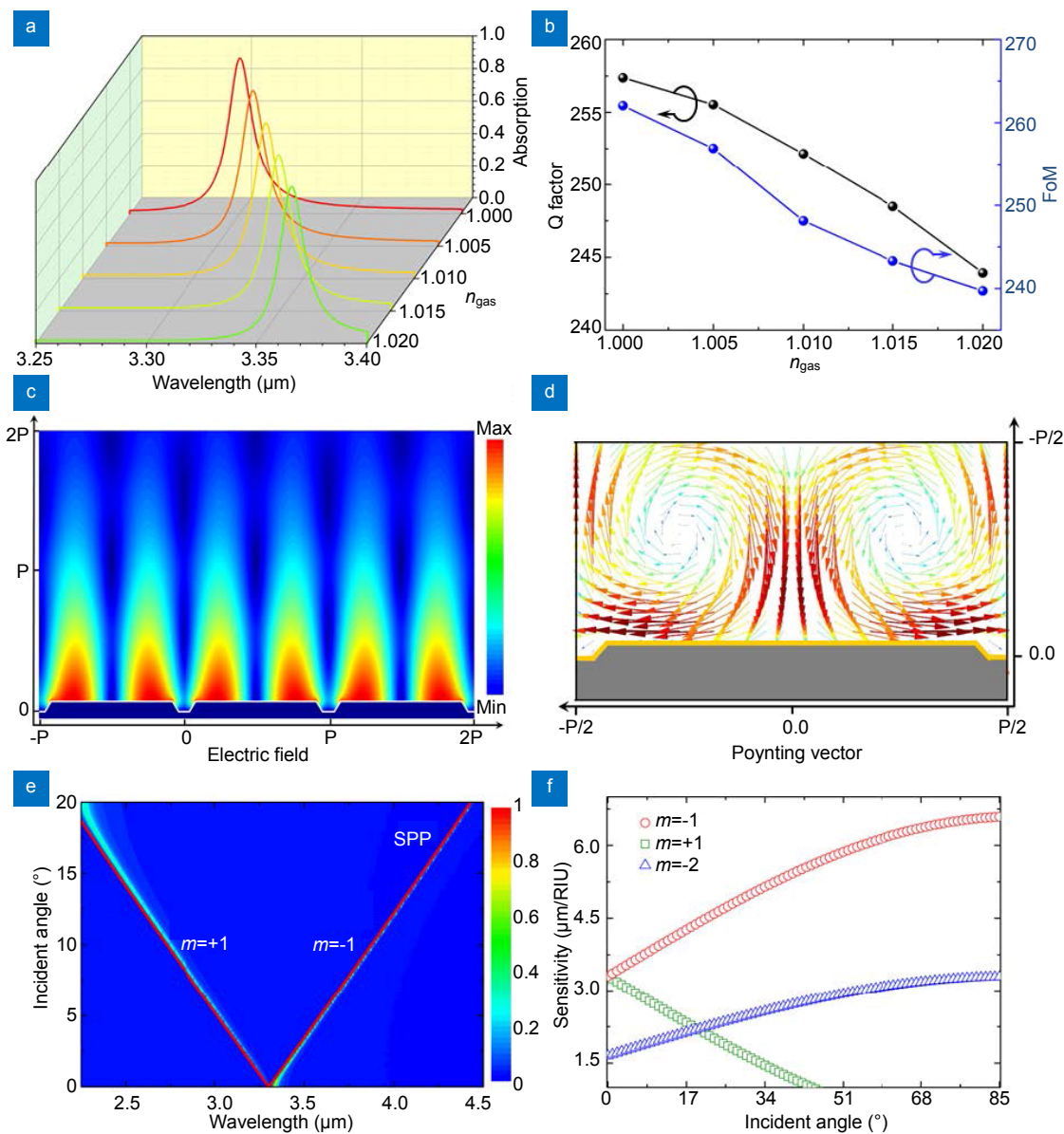
Fig. 2 | (a) Simulated absorption spectra at different n_{gas} for the device structure in Fig. 1(a). The period of gratings $P = 3.3$ μm, the grating depth $h_g = 160$ nm, and the grating width $w_g = (w_1+w_2)/2 = 3$ μm. **(b)** Q factor and FoM at various n_{gas}. **(c)** The electric field distribution at the resonance peak ($\lambda = 3.3$ μm) at $n_{gas} = 1$. **(d)** Poynting vector at the resonance. **(e)** The calculated absorption spectra as functions of wavelength and incident angle. **(f)** Sensitivities of different order modes versus the incident angle.

of magnitude larger than that of conventional plasmonic and metamaterials absorbers[42]. As a result, a figure of merit FoM=S/FWHM>200 and a FoM*= (dI/dn)/I>96 (I is the light intensity, dI is the variation of intensity for a change of RI dn) are achieved[52]. In contrast, the FoM and FoM* are 60 and 55, respectively, in plasmonic Mach-Zehnder interferometer gas sensor[53].

It is important to understand the physics governing the light coupling to the high Q surface resonant mode. In such a continuous metal film coated grating structure, propagating SPR modes are supported. Therefore, the resonance wavelength of the diffractive coupled surface propagating mode can be de determined by the momentum matching conditions:

$$k\sin(\theta_{in}) + mG = \pm k_{sp} \quad , \qquad (1)$$

where θ_{in} is the incident angle, $G=2\pi/P$ is the grating constant, $k=2\pi n_{gas}/\lambda$ is the wave vector, and k_{sp} is the wave vector of SPR mode. Since ultra-shallow ($H<\lambda/20$) grooves can be considered as very small perturbations to the flat metal surface, k_{sp} can be approximately calculated using the dispersion relationship of SPR mode supported by a flat Au/dielectric interface. In addition, m is an integer representing the diffraction order while '+' and '-' signs in the right side of the equation correspond to diffracted waves of orders $m>0$ (positive order) and $m<0$ (negative order), respectively. In Fig. 2(e), the resonance wavelength versus the incident angle predicted by SPR coupling formulas (Eq. (1)) is superimposed over the numerical absorption spectra of the multilayer grating structure. The theoretical prediction shows reasonable agreement with the numerical calculations with regards to the similar band shift upon changing incident angle or RI of the incident medium. The findings above offer a convincing proof that the observed absorption anomaly stems from the diffractive character of the periodic structures. It is interesting to quantitatively determine the theoretical maximum RI sensitivity for a specific diffraction order coupled SPP mode in such a device configuration. As illustrated in Fig. 2(f), the RI sensitivity at normal incidence is 3300 nm/RIU for the first diffraction order and decreases by half for the second order, which is close to $P/|m|$. As the angle of incidence increases, the diffractive coupled SPP mode splits into two modes linked to positive or negative orders. From Fig. 2(f), it is observed that the RI sensitivities of positive and negative orders have opposite dependency on the incident angle. With the increasing incident angle, the sensitivity of the negative

order grows while the one of the positive order reduces. For extremely large incident angles, the RI sensitivity of the first negative order mode is approaching a remarkable value of 6580 nm/RIU.

For on-chip electrical readout, it is preferred to have a high resonant light absorption so that large electrical output signal can be realized by the temperature variation associated with light absorption. As mentioned above, the maximum absorption occurs at the critical coupling condition when the radiation loss equals the absorption loss. By finely tuning the grating depth, high absorption above 96% at the resonances is obtained as shown in Fig. 2(a). Figure 2(d) shows the corresponding Poynting vector plot at the resonance for the critical coupling case. As indicated by the arrows, the electromagnetic energy flows are primarily trapped on the top of the gratings with the formation of the vortex-like Poynting vector profiles, resulting in the significantly suppressed reflection loss. In this scenario, most of the incident energy will be efficiently absorbed by the Au layer and generates heat that raises the temperature of the Au/Si$_3$N$_4$/VO$_2$/Si$_3$N$_4$/Si stack.

Thermal analysis

As described in the device mechanism, photothermal conversion is a key step to connect the gas induced light absorption to the on-chip electrical readout. There are two major factors for the efficient photothermal conversion in this proposed gas sensor. One is the heat capacity and the other is the heat dissipation. The smaller the heat capacity and the slower the heat dissipation, the higher temperature difference can be realized in the VO$_2$ layer, i.e. a higher sensing performance. An SOI wafer based fabrication process is straightforward in this case by integrating the transducer in the silicon device layer and removing the backside silicon handle layer to form a membrane. As shown in Fig. 3(a), the grating structure is fabricated on the silicon device layer and then covered with the Au/Si$_3$N$_4$/VO$_2$/Si$_3$N$_4$ stack. By removing the backside silicon handle layer, a combined sensing and transducing element is achieved including a multilayer stack of Au/Si$_3$N$_4$/VO$_2$/Si$_3$N$_4$/Si/SiO$_2$. This dual functional element is electrically connected with two electrodes on the surrounding silicon mesa by Au wires with a width of 20 μm. As seen, the transducer is surrounded by air in both up and down directions. Moreover, the heat dissipation channel in the plane is governed by the thin SiO$_2$ film. Therefore, it is expected to have an obvious temperature variation under illumination. The sensing area covers a
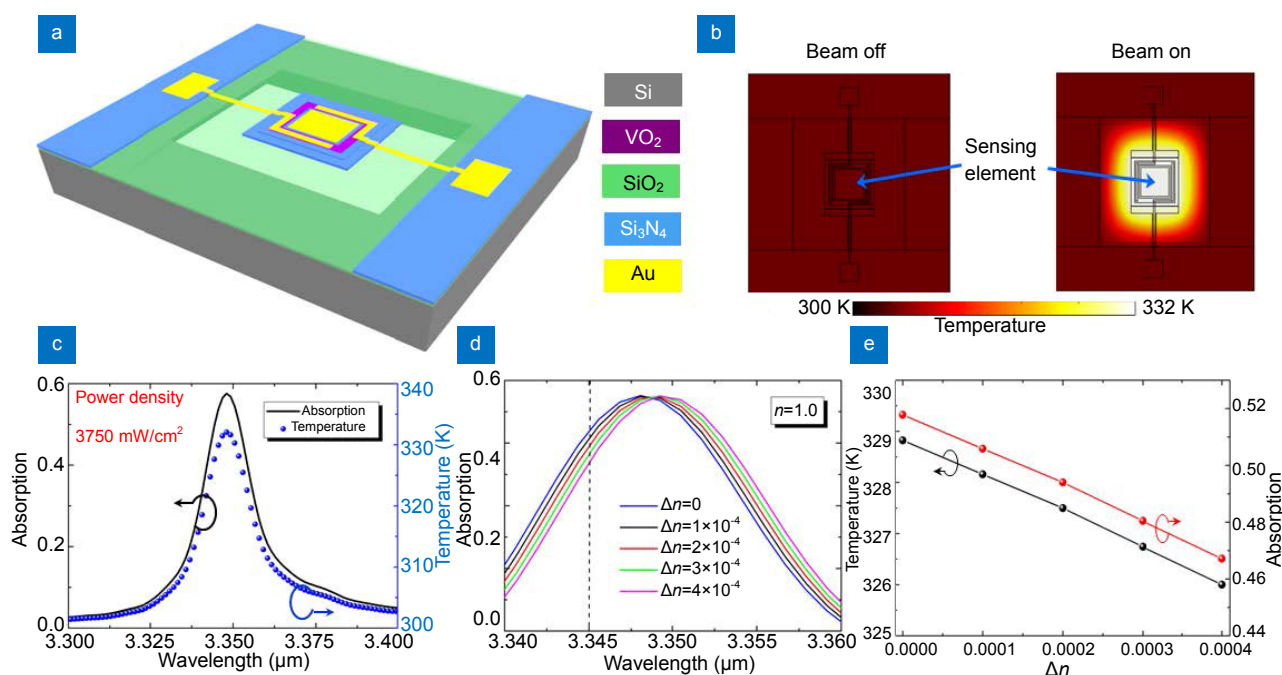
Fig. 3 | (**a**) Schematic of on-chip mid-IR gas sensor based on an SOI platform, where the silicon substrate in the area underneath the sensor is removed to reduce the thermal dissipation. The thickness of each layer in the Au/Si$_3$N$_4$/VO$_2$/Si$_3$N$_4$/Si stack is 200 nm, 50 nm, 100 nm, 500 nm and 4 μm, respectively. The thickness of the oxide layer is 1 μm. P = 3.3 μm, h_g = 220 nm, w_g = 3 μm. (**b**) Simulated temperature distribution across the sensor with the illumination on and off when the power density of light is 3.75 W/cm^2 at 3.348 μm and corresponding absorption efficiency is 58%. (**c**) Temperature maximum under different wavelength illumination at the same power density and the absorption spectra of the gratings. The period number of the grating is 100. (**d**) Absorption spectra for variation of different environmental RI. (**e**) Absorption at 3.345 μm illumination and the associated device temperature versus the variation of different environmental RI.

size of 330 μm × 330 μm, including 100 periods of gratings. There is a buffer area with 500 μm width between the sensing window and the surrounding mesa. In the thermal simulation, the grating region of the structure can be treated as a heat source with a power density determined by the illumination and light absorption from the optical simulation above. Open boundary conditions are set at the four lateral surfaces of the structure and convection boundary conditions are used for the rest, where the heat transfer coefficient is set to be 3 W/(m^2× K). The thermal conductivity and heat capacity of various materials are from the literature[54] and the material database of COMSOL software.

As shown in Fig. 3(c), the peak absorption is 58% due to the limited area (100 gratings) with a FWHM of 18 nm. Illuminated at a resonance wavelength of 3.348 μm, the active region shows a temperature distribution between 300 K and 332 K as shown in Fig. 3(b). By tuning the illumination wavelength, the temperature varies accordingly with the same trend of the absorption spectrum, which means that the photothermal effect is dominated by the surface mode of the grating structures. In fact, gas detection based on RI has a long history although the RI variation of gas with the concentration is not as large as

liquid. In 1982, SPP has been applied for halothane detection with the sensitivity of 3×10^{-5} deg/ppm[19]. Recently, an extremely low detection limit <10^{-8} RIU was demonstrated in a 30 mm all-fiber gas sensor[55]. It is interesting to know how much the temperature can be affected by the gas environment in the proposed sensor with a size less than 2 mm^2 and its sensitivity. As shown in Fig. 3(d), the resonance wavelength shifts from 3348.0 nm at n_{gas} = 1 to 3349.3 nm at n_{gas} = 1.0004, which indicates the wavelength sensitivity S = 3250 nm/RIU. Considering the spectral resolution (~0.5 cm^{-1}) of commercial Fourier transfer infrared (FTIR) spectrometers, it can measure a minimum RI change of 1.7×10^{-4} RIU that is much larger than the counterpart in the visible range. It is obviously not enough for gas sensing. With the resonance shift, the absorption changes as well. For example, the absorption at 3.345 μm decreases from 51.8% at n_{gas}=1 to 46.7% at n_{gas}=1.0004, with the amplitude sensitivity $S^*= \Delta I/\Delta n$ = 127.5%/RIU. This change of light absorption results in a temperature variation of 2.7 K as shown in Fig. 3(e). Considering the detection resolution of 30 mK of commercial VO$_2$ thermal detector[50], the RI detection limit of such an on-chip gas sensor is expected to be 4.4×10^{-6} RIU. This value gives a detection limit of approximately 29000 ppm

for CO_2 in a Ar/CO_2 mixture, which is compatible to previous works[33,34]. It is noted that the analysis of the sensing performance in this section only considers the real part of the gas RI, i.e. this technique can be carried out for all kinds of gases that have no absorption at this wavelength. The advantage is that the similar sensing experiment can be conducted for various gases without matching the laser source to the gas absorption peaks. In practical terms, there are requirements on low concentration gas detection or multiplexing gas detection from gas mixture. It is needed to further reduce the detection limit and improve the resolving capability. The former can be improved by optimized thermal design and gas enrichment strategy. The latter can be realized by matching the laser wavelength to the unique absorption peak of the target gas or enable on-chip spectroscopy by a transducer array.

Results and discussion

Thermal optimization and gas enrichment
To further improve the sensitivity, optimizing thermal design and introducing gas enrichment are both potential solutions. Actually, the device structure in Fig. 3(a) has relatively high heat dissipation via the large area membrane and it is not easy to fabricate an array of such a cell structure due to the wet etching for removing the silicon handle layer. Thus, an optimized air bridge structure commonly used in thermal focal plane array[56] are investigated, where the $Au/Si_3N_4/VO_2/Si_3N_4$ stack with gratings is supported by the Si_3N_4/W air bridge as shown in Fig. 4(a). This configuration provides an excellent thermal insulation due to the narrow heat dissipation path and is easy to form a transducer array for multiplex sensing or on-chip spectroscopy. The simulation setting is similar to the one in Fig. 3. As shown in Fig. 4(c), the temperature distributions clearly show the limited heat dissipation along the supporting arms and uniformity across the transducing element. For a transducer with a size of 330 μm (100 gratings) × 50 μm, the temperature of the membrane increases approximately 34°C if illuminated at a wavelength of 3.345 μm with a power density of 1 W/cm². Considering the smaller thermal source and the lower illumination power than that in Fig. 3(a), the heating efficiency is approximately 30 times higher. For the environment gas RI changing from 1 to 1.0004, the temperature variation is 3.5 K. Considering the temperature detection limit of 30 mK of conventional VO_2 thermal
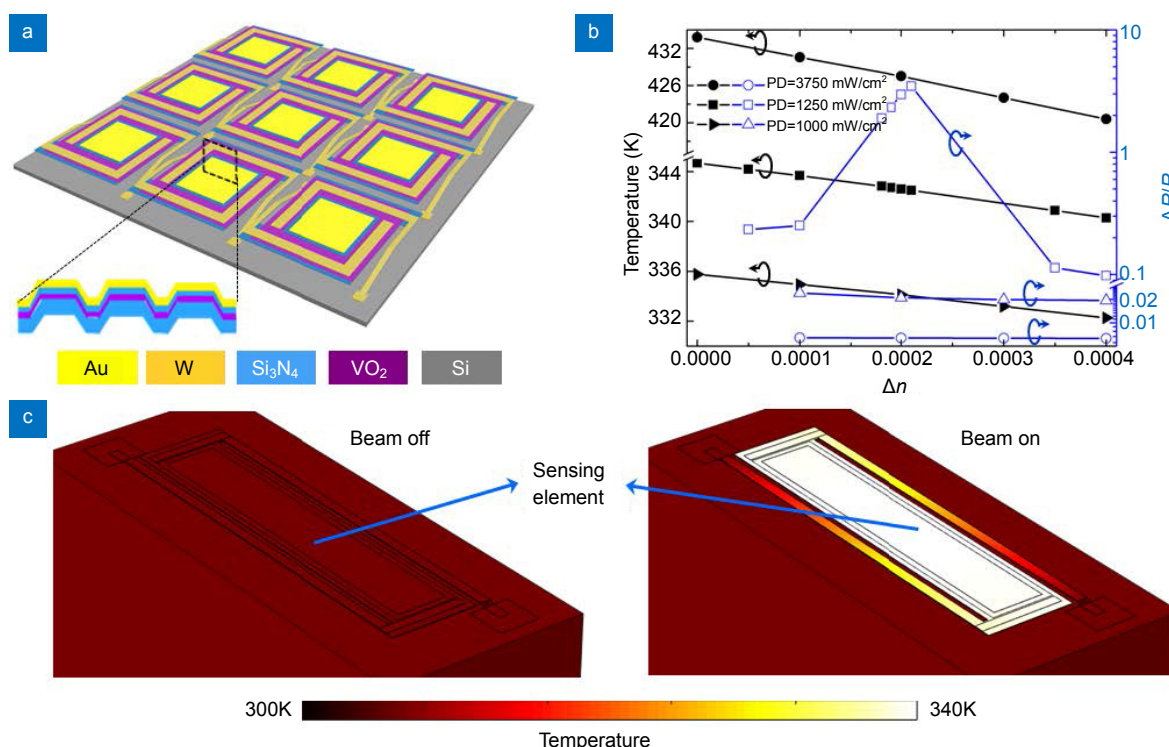
Fig. 4 | (**a**) Schematic of on-chip mid-IR gas sensor array based on an air bridge structure. The grating region has a size of 330 μm × 50 μm. The $Au/Si_3N_4/VO_2/Si_3N_4$ stack is shown in the inset and the thicknesses are 200 nm/50 nm/100 nm/500 nm, respectively. The stack is supported by the Si_3N_4/W bridges on Si substrate. (**b**) Temperature and relative electrical resistance variation of the sensors versus the variation of different environment gas RI. 'PD' means the power density of the incident light. (**c**) Simulated temperature distribution across the sensor with and without illumination at a wavelength of 3.348 μm with a power density of 1 W/cm² and the absorption is 58%.

detector[50], the RI sensing limit of this sensor is approximately 3.4×10^{-6} RIU for the device working at the semiconductor phase of VO_2. For a Ar/CO_2 mixture, a detection limit of 22550 ppm can be estimated from this value.

Absorptive gas sensing and on-chip spectroscopy

It is noted that only pure RI sensing is discussed above, which has no gas selection. The molecular absorption fingerprints of gases are actually very important for gas detection and identification. The common way is to choose a laser with an emission wavelength matching one absorption peak of the target gas and monitor the absorption variation. As discussion in literatures[23,33], MOF and polymer can be used to enrich the gas and thus increase the absorption. Gas enrichment technique was also used in refractive index sensing by coating MOF on metal nanoparticles[57]. Moreover, the greatly localized field of SPP as shown in Fig. 2(c) further improves the influence of the enriched gas in the MOF or polymer if it is close to the plasmonic structure. Similarly here, a MOF (zeolitic imidazolate framework, ZIF-8) with selective adsorption of CO_2[58] with a thickness of 2.7 μm is placed on top of the sensor. The void fraction of ZIFs is approximately 0.47[59]. The refractive index of the gas adsorbed MOF is given in Supplementary Information Section 2. In thermal simulation, the thermal conductivity and heat capacity at constant pressure of MOF are from literatures[60,61].

As shown in Fig. 5(a), the simulation shows that an absorption variation as high as 37% for 10% CO_2 in a Ar/CO_2 mixture can be obtained for the MOF and plasmonic absorber composite structure at 2.71 μm compared to 0.0046% for the pure CO_2 with the same optical

interaction length. As shown by the red and green lines, the pure RI variation in the real part induces a change of 27.8% in absorption, which is the working mechanism of sensors in Fig. 3 and 4. In addition, the absorption of CO_2 further enlarges the absorption variation shown by the blue line. As a result, in such a plasmonic absorber based gas sensor, both real and imaginary parts of RI of the target gas contribute to the sensing signal and thus improve the sensing performance by an enhancement factor as high as 8043. The performance may be further improved if the device is set to work at the CO_2 absorption peak for example 4.4 μm. As shown in Supplementary Information Section 3, it is easy to tune the device resonance to various gas absorption peaks. At the same illumination power and the membrane size as Fig. 4(b), the temperature raises by 31.44 K due to large absorption variation. Consequently, the detection limit of 95 ppm is evaluated considering the 30 mK resolution of conventional VO_2 detector. This value is very promising considering a very compact light-gas int eraction length of 2.7 μm in the proposed configuration that is three orders of magnitude smaller than the previous works[32,52]. Moreover, in the above case the VO_2 film is in the semiconductor phase. As shown in Fig. 4(b), if the illumination power increases to 1.25 W/cm² and 3.75 W/cm², the temperature of the membrane approaches 65 and 155°C respectively as shown in Fig. 4(b) and thus the VO_2 film is in the phase transition region and the metallic phase respectively. First, the rates of change in temperature at the same gas RI variation in phase transition region (33062 K/RIU) is about 4 times larger than that in the semiconductor phase (8745 K/RIU). Assuming the same temperature measuring res-
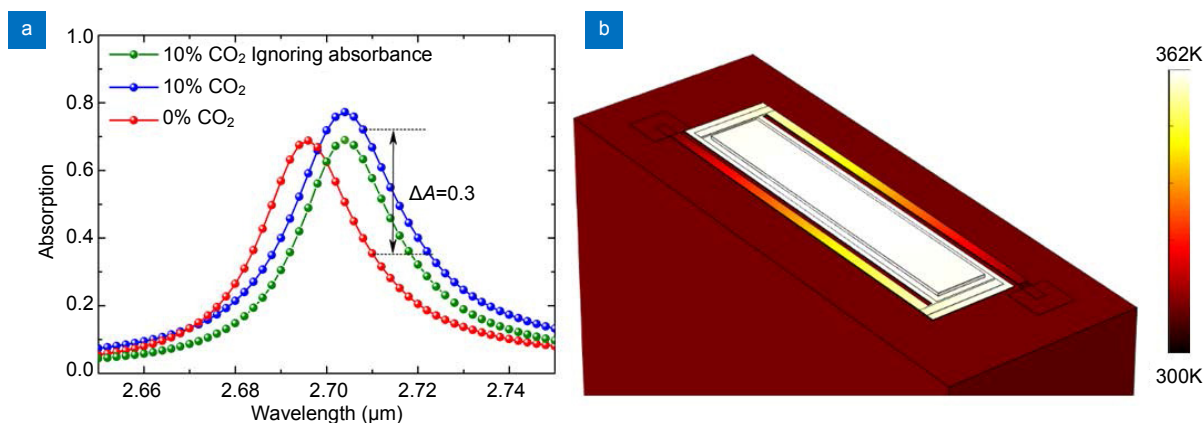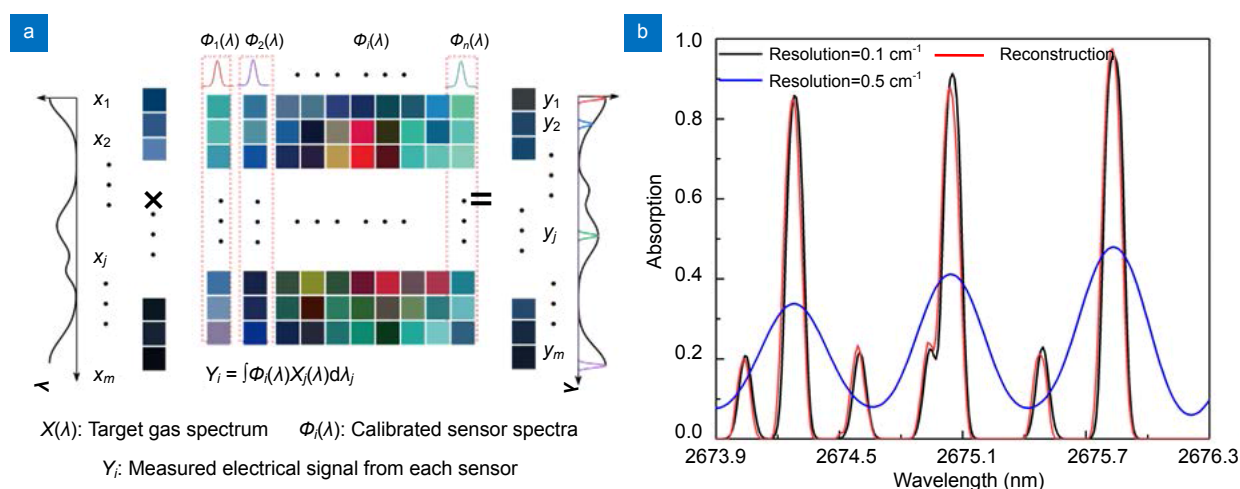

Fig. 5 | (**a**) Absorption spectra of a similar sensor as shown in Fig. 4 with an additional MOF layer placed on the top surface in pure Ar_2 and a mixture of $Ar(90\%)/CO_2(10\%)$. The result in a mixture of $Ar(90\%)/CO_2(10\%)$ ignoring the absorbance of CO_2 is also shown for comparison. $P = 1.99$ μm, $h_g = 100$ nm, $w_g = 1.25$ μm. RIs of CO_2 and MOF refer to literatures[57,60]. For a same membrane size (330 μm × 50 μm) with the one in Fig. 4, there are 165 gratings in this case. (**b**) Simulated temperature distribution across the sensor illuminated at a wavelength of 2.71 μm with a power density of 1 W/cm² in a mixture of $Ar(90\%)/CO_2(10\%)$.

olution, the gas concentration detection limit can be reduced to 24 ppm if the sensor is working at the VO_2 phase transition region. Moreover, the temperature resolution of 30 mK is for the VO_2 detector working in the semiconductor phase. As shown in Fig. 4(b), the relative electrical resistance variation in the phase transition region is two orders of magnitude larger than that in the semiconductor phase. Although a small working temperature range and the much lower temperature resolution are expected if the VO_2 thermal detection is developed in its phase transition region. As a result, a sub-ppm detection limit may be realized by all these strategies for extremely low concentration of target gas.

Although the narrowband detector and the MOF have some selectivity of target gas, the fault alarm could still occur using the non-dispersive method if different gases with similar absorption wavelengths or adsorption coefficients are mixed. Spectroscopy is an excellent way to address this issue because each gas has unique absorption fingerprints associated with the molecular rotation and vibrational frequency, but the current commercial spectrometers are too large and expensive for on-site application and the spectral resolution (0.5 cm^{-1}) is limited to resolve fine gas energy level. As the proposed plasmonic gas sensor has tunable absorption wavelength by simply changing the grating period, on-chip spectroscopy can be realized if a series of sensors with different absorption wavelengths are arranged into an array. Using a broadband source, each sensor detects the signal of the target gas absorption spectrum in a certain wavelength range. By combining all these signals, the whole absorption spectral information can be obtained by using the com-

pressive sensing algorithm (Fig. 6(a)), resulting in significantly improved spectral resolution[62–67]. For example, quantum dot absorptive filters[63], plasmonic grating filters[64] and multimode fibers[62] have been explored to construct the microspectrometer. To verify this idea, 80 gas sensors similar to the one in Fig. 4(a) are designed with the spectral response shown in Fig. S3(c), which can be patterned in a single lithography process step. The spectra of illumination source, CO_2 absorption and 80 sensors are given in Supplementary Information Section 4. Generally, the resonance linewidths of these absorption spectra are approximately 10 nm (0.014 cm^{-1}), but their spectral resolution can be very high by calibrating via tunable QCLs. The CO_2 molecular absorption coefficient (red line in Fig. S3(b)) is obtained from the HITRAN database[59]. The black and blue lines in Fig. 6(b) are simulated via a Gaussian model with a setting of spectral resolution of 0.5 cm^{-1} and 0.1 cm^{-1}, i.e., they mimic the measured spectra of FTIR at the corresponding resolution. As seen, there are actually 7 peaks between 2673.9 nm to 2676.3 nm with an average linewidth of the absorption peaks of approximately 0.1 nm, which is far beyond the capability of the state-of-the-art spectrometer (0.5 cm^{-1}). The mimic measured spectrum at a resolution of 0.5 cm^{-1} cannot accurately resolve each absorption peak. Please note that the resolution of 0.1 cm^{-1} is beyond the state-of-the-art of FTIR. To reconstruct the fingerprint absorption spectrum using the sensor array, first the integrations of the broadband source spectrum, CO_2 absorption spectrum and the sensor spectral responses are calculated, which in fact associate with the electrical readouts of the sensor array. Similar data without CO_2 absorption can also be obtained.

$X(\lambda)$: Target gas spectrum $\Phi_i(\lambda)$: Calibrated sensor spectra

Y_i: Measured electrical signal from each sensor

$Y_i = \int \Phi_i(\lambda) X_j(\lambda) d\lambda_j$

Fig. 6 | Gas molecular fingerprint spectrum reconstruction with the monolithically integrated plasmonic gas sensor array $\Phi(\lambda)$. (a) Schematic of the reconstruction process for an unknown input signal $X(\lambda)$, where the photoelectric signal Y of each sensor is recorded. (b) The recovered spectrum (red line) and the reference spectra by simulation based on HITRAN database (black and blue lines).

Using the L1 minimization algorithm, the CO_2 molecular absorption spectrum can be reconstructed with the calibrated sensor spectral response and the two integration array above (Fig. 6(b)). As seen, the reconstructed spectrum almost overlaps with the original signal with the resolution of approximately 0.01 nm that is far better than the commercial spectrometer. Therefore, the proposed mid-IR gas sensing technique not only provides potential high sensitivity for gas sensing but also an excellent on-chip spectroscopic function for fingerprint identification. Note that the spectral resolution of such technique associates with quite a few factors including the spectral correlation between the adopted filters, the accuracy of the calibrated filtering responses, the reconstruction algorithm itself, etc. Moreover, the actual measured spectral resolution is largely limited by various noises in the measuring system. It is found that the noise tolerance highly depends on the algorithm used for the signal recovery, which can be improved by using a quadratic instead of the equality constraint[68].

As seen, a large number of sensors in an array are required to construct the spectra although the number can be further reduced by optimizing the reconstruction algorithm. It is also preferred to reduce the size of each sensor to improve the mechanical stability of the membrane structure. In our case each sensor has a sensing area of 330 μm× 50 μm at a cost of absorption as shown in Fig. 3(c) and that in literature[35] is even 1000 μm × 1000 μm. It is important to know the fundamental reason of the size effect and find a way to solve it. As discussed in Fig. 2(e), the light absorption is dominated by the SPP mode. The incident light is coupled into the in-plane surface wave by the gratings and absorbed during its propagation along the metal surface. If the grating region is not large enough to cover the attenuation length of the surface wave, the light absorption is not complete, which is the reason of the reduced absorption. This value is further reduced to 30% if there are only 60 periods as shown in Fig. S4. This size effect exists at any wavelength range and is worse in the structure with a larger Q factor. As seen, the absorption drops from 93% to 60% when the grating number is reduced to 50 in a wavelength range around 9 μm as shown in Fig. S4(b). There are two ways to reduce the size of transducer element without sacrificing the resonant absorption. One is to increase the attenuation coefficient such as using lossy materials and the other is to increase the effective propagating length of the surface wave such as adopting a lateral cavity, both of

which increases the absorption at a certain device size. However, the former is not preferred because it reduces the Q factor of the resonance simultaneously. Alternatively, the latter can be realized by adding two reflective structures at both ends of the gratings as shown in the inset of Fig. S4(c). By fabricating a metal coated step with a depth h=9.9 μm at both ends of the gratings, the resonant absorption reaches as high as 88%. This remarkable suppression of the size effect comes from the efficient reflection of the surface propagating mode. As shown in Fig. 2(c), the main out-of-plane field of the surface propagating mode extends to a distance more than one period of the grating. Thus, the depth of the reflectors should be larger than one period. If the reflectors are too small to reflect all the surface propagating modes as shown by the blue and red lines in Fig. S4(c), the light absorption drops. In addition, the length of the transducing elements along the grating direction can be further reduced as well. As shown in Fig. S4(d), a length of 5 μm is enough to ensure a high absorption efficiency above 85%. Therefore, the transducing element can be as small as 50 μm × 5 μm, which is more than 400 times smaller than the sensing region in Fig. 3(a) and very important for multiplexing and on-chip spectroscopy. How to fabricate such a structure is still an open question for future work.

Conclusions

In conclusion, we proposed and demonstrated numerically a novel plasmonic mid-IR gas sensor, which shows a remarkable gas absorption enhancement factor over 8000 in an ultracompact optical interaction length of only several microns. Moreover, on-chip readout and spectroscopy have been achieved by integrating optical sensing, photothermal detection and compressive sensing algorithm. In particular, the estimated spectral resolution as high as 0.01 nm is quite promising to use in gas identification with such a portable device. The unity integration idea of active and passive optical components provides a novel technique for on-chip sensing. The shallow metal grating structure in the proposed sensor also provide an excellent platform combining both localized electromagnetic field and high Q factor.

References

1. Gibson D, MacGregor C. A novel solid state non-dispersive infrared CO_2 gas sensor compatible with wireless and portable deployment. *Sensors* **13**, 7079–7103 (2013).
2. Caron A, Redon N, Thevenet F, Hanoune B, Coddeville P. Performances and limitations of electronic gas sensors to in-

vestigate an indoor air quality event. *Build Environ* **107**, 19–28 (2016).

3. Narayanan S, Rice G, Agah M. A micro-discharge photoionization detector for micro-gas chromatography. *Microchim Acta* **181**, 493–499 (2014).

4. Barreca D, Bekermann D, Comini E, Devi A, Fischer R A et al. 1D ZnO nano-assemblies by Plasma-CVD as chemical sensors for flammable and toxic gases. *Sens Actuators B: Chem* **149**, 1–7 (2010).

5. Güntner A T, Pineau N J, Chie D, Krumeich F, Pratsinis S E. Selective sensing of isoprene by Ti-doped ZnO for breath diagnostics. *J Mater Chem B* **4**, 5358–5366 (2016).

6. Priyanka K P, Vattappalam S C, Sankararaman S, Balakrishna K M, Varghese T. High-performance ethanol gas sensor using TiO_2 nanostructures. *Eur Phys J Plus* **132**, 306 (2017).

7. Liu X, Cheng S T, Liu H, Hu S, Zhang D Q et al. A survey on gas sensing technology. *Sensors* **12**, 9635–9665 (2012).

8. Ma N, Suematsu K, Yuasa M, Kida T, Shimanoe K. Effect of water vapor on Pd-Loaded SnO_2 nanoparticles gas sensor. *ACS Appl Mater Interfaces* **7**, 5863–5869 (2015).

9. Piriya V S A, Joseph P, Daniel S C G K, Lakshmanan S, Kinoshita T et al. Colorimetric sensors for rapid detection of various analytes. *Mater Sci Eng: C* **78**, 1231–1245 (2017).

10. Wang S Y, Ma J Y, Li Z J, Su H Q, Alkurd N R et al. Surface acoustic wave ammonia sensor based on ZnO/SiO_2 composite film. *J Hazard Mater* **285**, 368–374 (2015).

11. Lochbaum A, Fedoryshyn Y, Dorodnyy A, Koch U, Hafner C et al. On-chip narrowband thermal emitter for Mid-IR optical gas sensing. *ACS Photonics* **4**, 1371–1380 (2017).

12. Zheng Y, Wu Z F, Shum P P, Xu Z L, Keiser G et al. Sensing and lasing applications of whispering gallery mode microresonators. *Opto-Electron Adv* **1**, 180015 (2018).

13. Deng C S, Li M J, Peng J, Liu W L, Zhong J X. Simultaneously high-Q and high-sensitivity slotted photonic crystal nanofiber cavity for complex refractive index sensing. *J Opt Soc Am B* **34**, 1624–1631 (2017).

14. Moumen S, Raible I, Krauß A, Wöllenstein J. Infrared investigation of CO_2 sorption by amine based materials for the development of a NDIR CO_2 sensor. *Sens Actuators B: Chem* **236**, 1083–1090 (2016).

15. Lackner M. Tunable diode laser absorption spectroscopy (TDLAS) in the process industries–a review. *Rev Chem Eng* **23**, 65 (2007).

16. Tong J C, Suo F, Ma J H Z, Tobing L Y M, Qian L et al. Surface plasmon enhanced infrared photodetection. *Opto-Electron Adv* **2**, 180026 (2019).

17. Bingham J M, Anker J N, Kreno L E, Van Duyne R P. Gas sensing with high-resolution localized surface plasmon resonance spectroscopy. *J Am Chem Soc* **132**, 17358–17359 (2010).

18. Jágerská J, Le Thomas N, Zhang H, Diao Z, Houdre R. Refractive index gas sensing in a hollow photonic crystal cavity. In *Proceedings of 2010 12th International Conference on Transparent Optical Networks* 1–4 (IEEE, 2010); http://doi.org/10.1109/ICTON.2010.5549037.

19. Nylander C, Liedberg B, Lind T. Gas detection by means of surface plasmon resonance. *Sens Actuators* **3**, 79–88 (1982–1983).

20. Liu N, Tang M L, Hentschel M, Giessen H, Alivisatos A P. Nanoantenna-enhanced gas sensing in a single tailored nanofocus. *Nat Mater* **10**, 631–636 (2011).

21. Allsop T, Arif R, Neal R, Kalli K, Kundrát V et al. Photonic gas sensors exploiting directly the optical properties of hybrid carbon nanotube localized surface plasmon structures. *Light: Sci Appl* **5**, e16036 (2016).

22. Li Y X, Chen N, Deng D Y, Xing X X, Xiao X C et al. Formaldehyde detection: SnO_2 microspheres for formaldehyde gas sensor with high sensitivity, fast response/recovery and good selectivity. *Sens Actuators B: Chem* **238**, 264–273 (2017).

23. Hasan D, Lee C. Hybrid metamaterial absorber platform for sensing of CO_2 gas at Mid‐IR. *Adv Sci* **5**, 1700581 (2018).

24. Werle P, Popov A. Application of antimonide lasers for gas sensing in the 3–4-μm range. *Appl Opt* **38**, 1494–1501 (1999).

25. Charlton C, De Melas F, Inberg A, Croitoru N, Mizaikoff B. Hollow-waveguide gas sensing with room-temperature quantum cascade lasers. *IEE Proc-Optoelectron* **150**, 306–309 (2003).

26. Zhang Y, Gao W Z, Song Z Y, An Y P, Li L et al. Design of a novel gas sensor structure based on mid-infrared absorption spectrum. *Sens Actuators B: Chem* **147**, 5–9 (2010).

27. Liang L, Hu X, Wen L, Zhu Y H, Yang X G et al. Unity integration of grating slot waveguide and microfluid for terahertz sensing. *Laser Photonics Rev* **12**, 1800078 (2018).

28. Wen L, Liang L, Yang X G, Liu Z, Li B J et al. Multiband and ultrahigh figure-of-merit nanoplasmonic sensing with direct electrical readout in Au-Si nanojunctions. *ACS Nano* **13**, 6963–6972 (2019).

29. Hu X, Xu G Q, Wen L, Wang H C, Zhao Y C et al. Metamaterial absorber integrated microfluidic terahertz sensors. *Laser Photonics Rev* **10**, 962–969 (2016).

30. Yesilkoy F, Arvelo E R, Jahani Y, Liu M K, Tittl A et al. Ultrasensitive hyperspectral imaging and biodetection enabled by dielectric metasurfaces. *Nat Photonics* **13**, 390–396 (2019).

31. Matuschek M, Singh D P, Jeong H H, Nesterov M, Weiss T et al. Chiral plasmonic hydrogen sensors. *Small* **14**, 1702990 (2018).

32. Tan Z X, Hao H, Shao Y H, Chen Y Z, Li X J et al. Phase modulation and structural effects in a D-shaped all-solid photonic crystal fiber surface plasmon resonance sensor. *Opt Express* **22**, 15049–15063 (2014).

33. Chong X Y, Kim K J, Zhang Y J, Li E W, Ohodnicki P R et al. Plasmonic nanopatch array with integrated metal–organic framework for enhanced infrared absorption gas sensing. *Nanotechnology* **28**, 26LT01 (2017).

34. Pusch A, De Luca A, Oh S S, Wuestner S, Roschuk T et al. A highly efficient CMOS nanoplasmonic crystal enhanced slow-wave thermal emitter improves infrared gas-sensing devices. *Sci Rep* **5**, 17451 (2015).

35. Tan X C, Li J Y, Yang A, Liu H, Yi F. Narrowband plasmonic metamaterial absorber integrated pyroelectric detectors towards infrared gas sensing. *Proc SPIE* **10536**, 105361H (2018.)

36. Genner A, Gasser C, Moser H, Ofner J, Schreiber J et al. On-line monitoring of methanol and methyl formate in the exhaust gas of an industrial formaldehyde production plant by a mid-IR gas sensor based on tunable Fabry-Pérot filter technology. *Anal Bioanal Chem* **409**, 753–761 (2017).

37. Rück T, Bierl R, Matysik F M. Low-cost photoacoustic NO_2 trace gas monitoring at the pptV-level. *Sens Actuators A: Phys* **263**, 501–509 (2017).

38. Yin X K, Dong L, Wu H P, Zhang L, Ma W G et al. Highly sensitive photoacoustic multicomponent gas sensor for SF_6 decom-

position online monitoring. *Opt Express* **27**, A224–A234 (2019).

39. Wen L, Chen Q, Hu X, Wang H C, Jin L, Su Q. Multifunctional silicon optoelectronics integrated with plasmonic scattering color. *ACS Nano* **10**, 11076–11086 (2016).

40. Delli E, Letka V, Hodgson P D, Repiso E, Hayton J P et al. Mid-infrared InAs/InAsSb superlattice nBn photodetector monolithically integrated onto silicon. *ACS Photonics* **6**, 538–544 (2019).

41. Sassi U, Parret R, Nanot S, Bruna M, Borini S et al. Graphene-based mid-infrared room-temperature pyroelectric bolometers with ultrahigh temperature coefficient of resistance. *Nat Commun* **8**, 14311 (2017).

42. Liu N, Mesch M, Weiss T, Hentschel M, Giessen H. Infrared perfect absorber and its application as plasmonic sensor. *Nano Lett* **10**, 2342–2348 (2010).

43. Sobhani A, Knight M W, Wang Y M, Zheng B, King N S et al. Narrowband photodetection in the near-infrared with a plasmon-induced hot electron device. *Nat Commun* **4**, 1643 (2013).

44. Singh R, Cao W, Al-Naib I, Cong L Q, Withayachumnankul W et al. Ultrasensitive terahertz sensing with high-*Q* Fano resonances in metasurfaces. *Appl Phys Lett* **105**, 171101 (2014).

45. Debus C, Bolivar P H. Frequency selective surfaces for high sensitivity terahertz sensing. *Appl Phys Lett* **91**, 184102 (2007).

46. Tamagnone M, Ambrosio A, Chaudhary K, Jauregui L A, Kim P et al. Ultra-confined mid-infrared resonant phonon polaritons in van der Waals nanostructures. *Sci Adv* **4**, eaat7189 (2018).

47. Qu C, Ma S J, Hao J M, Qiu M, Li X et al. Tailor the functionalities of metasurfaces based on a complete phase diagram. *Phys Rev Lett* **115**, 235503 (2015).

48. Kocer H, Butun S, Banar B, Wang K, Tongay S et al. Thermal tuning of infrared resonant absorbers based on hybrid gold-VO$_2$ nanostructures. *Appl Phys Lett* **106**, 161104 (2015).

49. Lv J, Que L C, Wei L H, Zhou Y, Liao B B et al. Uncooled microbolometer infrared focal plane array without substrate temperature stabilization. *IEEE Sens J* **14**, 1533–1544 (2014).

50. Niklaus F, Vieider C, Jakobsen H. MEMS-based uncooled infrared bolometer arrays: a review. *Proc SPIE* **6836**, 68360D (2007).

51. Palik E D. *Handbook of Optical Constants of Solids* (Academic Press, San Diego, 1998).

52. Cheng F, Yang X D, Gao J. Enhancing intensity and refractive index sensing capability with infrared plasmonic perfect absorbers. *Opt Lett* **39**, 3185–3188 (2014).

53. Sherif S M, Swillam M A. Metal-less silicon plasmonic mid-infrared gas sensor. *J Nanophotonics* **10**, 026025 (2016).

54. Ordonez-Miranda J, Ezzahri Y, Joulain K, Drevillon J, Alvarado-Gil J J. Modeling of the electrical conductivity, thermal conductivity, and specific heat capacity of VO$_2$. *Phys Rev B* **98**, 075144 (2018).

55. Pevec S, Donlagic D. Miniature fiber-optic Fabry-Perot refractive index sensor for gas sensing with a resolution of 5×10^{-9} RIU. *Opt Express* **26**, 23868–23882 (2018).

56. Rogalski A. Progress in focal plane array technologies. *Prog Quant Electron* **36**, 342–473 (2012).

57. Kreno L E, Hupp J T, Van Duyne R P. Metal−organic framework thin film for enhanced localized surface plasmon resonance gas sensing. *Anal Chem* **82**, 8042–8046 (2010).

58. Chong X Y, Zhang Y J, Li E W, Kim K J, Ohodnicki P R et al. Surface-enhanced infrared absorption: pushing the frontier for on-chip gas sensing. *ACS Sens* **3**, 230–238 (2018).

59. Thornton A W, Simon CM, Kim J, Kwon O, Deeg K S et al. Materials genome in action: identifying the performance limits of physical hydrogen storage. *Chem Mater* **29**, 2844–2854 (2017).

60. Rothman L S, Gordon I E, Barbe A, Benner D C, Bernath P F et al. The *HITRAN* 2008 molecular spectroscopic database. *J Quant Spectrosc Radiat Transfer* **110**, 533–572 (2009).

61. Zhang X L, Jiang J W. Thermal conductivity of zeolitic imidazolate framework-8: A molecular simulation study. *J Phys Chem C* **117**, 18441–18447 (2013).

62. Calvin J J, Rosen P F, Smith S J, Woodfield B F. Heat capacities and thermodynamic functions of the ZIF organic linkers imidazole, 2-methylimidazole, and 2-ethylimidazole. *J Chem Thermodyn* **132**, 129–141 (2019).

63. Redding B, Alam M, Seifert M, Cao H. High-resolution and broadband all-fiber spectrometers. *Optica* **1**, 175–180 (2014).

64. Bao J, Bawendi M G. A colloidal quantum dot spectrometer. *Nature* **523**, 67–70 (2015).

65. Li E W, Chong X Y, Ren F H, Wang A X. Broadband on-chip near-infrared spectroscopy based on a plasmonic grating filter array. *Opt Lett* **41**, 1913–1916 (2016).

66. Cerjan B, Halas N J. Toward a nanophotonic nose: a compressive sensing-enhanced, optoelectronic mid-infrared spectrometer. *ACS Photonics* **6**, 79–86 (2019).

67. Wang Z, Yi S, Chen A, Zhou M, Luk T S et al. Single-shot on-chip spectral sensors based on photonic crystal slabs. *Nat Commun* **10**, 1020 (2019).

68. Wang Z, Yu Z F. Spectral analysis based on compressive sensing in nanophotonic structures. *Opt Express* **22**, 25608–25614 (2014).

Acknowledgements

Author contributions

Q. Chen and L. Wen conceived the work and proposed the design. L. Liang, L. Wen and Q. L. Zheng conducted the simulation. Q. Chen wrote the paper. All authors discussed the results and commented on the manuscript.

Competing interests

The authors declare no competing financial interests.

Supplementary information

Supplementary information for this paper is available at
https://doi.org/10.29026/oea.2020.190040